Stability Analysis of Multi-terminal HVDC with Diode Rectifier connected Off-shore Wind Power Plants

S. Bernal-Perez[a], S. Añó-Villalba[a,*], R. Blasco-Gimenez[a]

[a]*Universitat Politècnica de València, 46022 Valencia, Spain*

Abstract

This paper addresses the detailed modeling and small-signal stability analysis of a multi-terminal high voltage direct current (HVDC) system including a large diode rectifier-connected off-shore wind power plant (WPP). The study covers both islanded and connected WPP operation with different control scenarios. Islanded WPP stands for non-conducting HVDC diode rectifier (DR) whereas in connected WPP operation the DR is conducting. The study of both modes is important as the WPP would be in one of these modes during normal operation.

Variable off-shore ac-grid frequency and a dynamic diode rectifier model have been considered for adequate dynamic modeling. The proposed models have been validated against detailed PSCAD EMT simulations and have been used to carry out the small-signal stability analysis of the islanded and connected WPP with different scenarios. Moreover, the dynamic model is used to assess the system robustness against parametric uncertainties, communication delay and power level, ensuring the integration of the off-shore WPP into the on-shore electrical power system. This study also points out that adequate droop control of the HVDC grid has a larger impact on overall stability than the diode rectifier connected off-shore WPP controllers.

Keywords:

Wind power generation, HVDC diode rectifier (DR), HVDC link control, voltage source converter (VSC), small-signal stability analysis.

Nomenclature

Subscrips

d	d-component of Park transformation
i	Index to wind turbine cluster ($i = 1, 2, .., 5$)
j	Multiterminal HVDC: index to VSC station ($j = 1, 2, 3$)

---

*Corresponding author (sanyo@die.upv.es).

q q-component of Park transformation

Variables

ω_F Diode rectifier: ac-filter angular frequency

ω_S On-shore ac-grid PCC angular frequency

E_{Bi} Wind turbine cluster-i: dc-link voltage

E_C HVDC cable T-model: C_C capacitor voltage

E_H Multiterminal HVDC: radial grid common voltage

E_I HVDC submarine cable receiving-end voltage

E_R HVDC submarine cable sending-end voltage

I_{FR} Diode rectifier ac-filter: Z_{FR} input current

I_F Wind power plant output current

I_{Hj} Multiterminal HVDC grid: VSC-j cable sending-end current

I_H Multiterminal HVDC grid: diode rectifier cable receiving-end current

I_{Idc} HVDC submarine cable receiving-end current

I_{La} Diode rectifier ac-filter: L_a inductor current

I_{Lb} Diode rectifier ac-filter: L_b inductor current

I_{Rac} Diode rectifier ac-filter: Z_{FR} output current

I_{Rdc} Diode rectifier output dc-current

I_S On-shore ac-grid input current

I_V HVDC VSC output ac-current

I_{Wi} Wind turbine cluster-i: front-end output ac-current

P_{Fi} Wind turbine cluster-i: active output power

P_F Wind power plant active output power

P_{Idc} HVDC submarine cable receiving-end power

P_{Rdc} Diode rectifier output power

P_{VS} HVDC VSC transformer: output active power

Q_{Fi} Wind turbine cluster-i: reactive output power

Q_F Wind power plant reactive output power

Q_{VS} HVDC VSC transformer: output reactive power

V_{Ca1} Diode rectifier ac-filter: C_{a1} capacitor voltage

V_{Ca2} Diode rectifier ac-filter: C_{a2} capacitor voltage

V_{Cb} Diode rectifier ac-filter: C_b capacitor voltage

V_F Diode rectifier: ac-filter voltage

V_{Rdc} Diode rectifier dc-voltage

V_{SG} On-shore ac-grid: Thevenin's equivalent voltage

V_S On-shore ac-grid input voltage

V_V HVDC VSC output voltage

V_{Wi} Wind turbine cluster-i: front-end output voltage

1. Introduction

HVDC links have been extensively used in the North Sea for the connection of distant, large-scale off-shore wind power plants (WPPs) [1, 2].

The coordinated design of wind turbine (WT) control, off-shore ac-grid, and HVDC link allows for the use of diode-based HVDC rectifiers for the connection of large WPPs to the on-shore ac-network, i.e, only DR-enabled WTs can be connected to DR stations. This grid connection solution offers large savings on both installation and operation costs [3, 4, 5]. An integrated transformer-diode based HVDC rectifier solution for the reduction of overall connection costs of distant off-shore WPPs has been proposed in [6, 7].

When the rectifier station of an HVDC link is an active element, it provides control on the ac-grid, e.g., a line-commutated rectifier can control its output current. Diode rectifier units lack control capability, therefore, the off-shore ac-grid voltage, frequency and power flow have to be controlled by the WTs as in [4, 8], where the control strategies ensures good performance for both steady-state and transient scenarios. The coordinated design of the WT and HVDC link has shown that a diode-based HVDC rectifier can be used in a droop-controlled HVDC grid, [9].

To ensure robust operation and integration of the complete system into the on-shore ac transmission network, small-signal stability and robustness analysis still remain to be addressed.

Previous researchers have carried out the stability analysis of line-commutated HVDC links [10] and [11], where a point-to-point line-commutated converter (LCC) HVDC connection of an off-shore WPP is studied. Modal control analysis is carried out for damping improvement of the current controllers. The rectifier station is modeled using a detailed dynamic model considering a constant off-shore ac-grid frequency.

The small-signal stability analysis of a point-to-point HVDC link is addressed in [12] and [13]. In [12], the stations are of VSC type and a selection of subsystems is performed in order to identify the origin of instabilities. As in [13], the stability analysis considers the measurement of the ac-frequency using a phase-locked loop (PLL).

The multi-terminal HVDC small-signal stability analysis is addressed in [14] and [15]. In [14] an averaged VSC model is used to analyze the stability of the multi-terminal HVDC integrated into a multi-machine ac-network. A four-terminal VSC based system is presented in [15] where the WPPs are of fixed-speed with induction generators.

3

The aforementioned studies did not consider the use of HVDC diode rectifier DR stations. To the authors knowledge, the only published stability analysis of a point-to-point HVDC diode rectifier connected off-shore WPP was carried out in [16] and recently in [17]. However, [16] included only point-to-point links and did not cover important aspects required for an accurate model, namely, the use of a precise dynamic model of the diode rectifier unit, the influence of the on-shore grid and a thorough validation against EMT (PSCAD) models.

In [17] a small-signal analysis of an HVDC rectifier (LCC and diode types) is performed for controller design. An LCC converter average-value model was presented for a point-to-point link, however the WPP model is too simplistic, as it is modeled as just a 3-phase current source, and therefore the ac-grid frequency is constant.

Therefore, this paper aims at providing accurate dynamic models for the small-signal analysis of DR-connected WPP to multi-terminal HVDC grids. In order to provide accurate dynamic models, this paper compares both constant and variable ac-grid frequency models, as well as averaged static and dynamic models of the diode rectifier unit. This paper includes the robustness analysis of the system against parametric uncertainties, communication delay and power level.

The methodology proposed for the small-signal analysis makes use of the different operating scenarios of the WPP with increasing complexity. Additionally, a participation factor analysis has been carried out in order to ascertain the influence of each state variable on poorly damped eigenvalues.

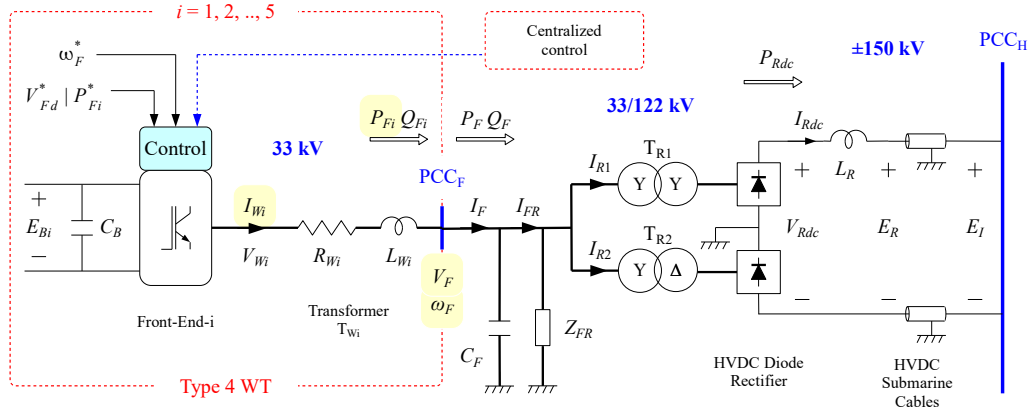## 2. Diode Rectifier-Connected Wind Power Plant

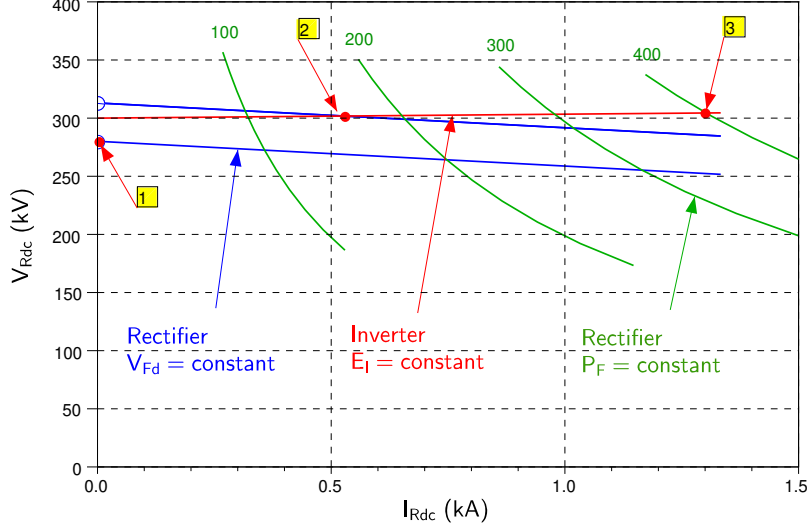Figure 1: Wind power plant connected to the HVDC link through an HVDC diode rectifier.

4

Figure 2: Steady-state operation of the HVDC link. 1: Islanded WPP, 2: WPP with voltage control, 3: WPP with power control.

2.1. System Description

Figure 1 shows the diagram of a diode rectifier-connected wind power plant. The off-shore WPP consists of 80 type-4 WTs each rated at 5 MW, totaling 400 MW. For ease of simulation and modeling, the WPP is split into five aggregated WT clusters of different rating: 5, 40, 80, 120 and 155 MW.

The WT grid converters (front-ends) are connected to the point of common coupling PCC_H through the step-up transformers T_{Wi}, $i = 1, 2, .., 5$, the uncontrolled HVDC rectifier and the submarine cables.

The HVDC diode rectifier (DR) consists of a 12-pulse bipolar station. C_F and Z_{FR} are the reactive power compensation and filter banks of the rectifier ac-side. L_R is the dc smoothing reactor.

The details and validation of the control strategies can be found in [4, 8], including the performance of the WPP to off-shore and on-shore short-circuits. System parameter values can be found in Appendix C.

2.2. Scenarios and Operating Points

Figure 2 illustrates the scenarios analyzed in this paper where the WPP is connected to an on-shore VSC inverter through the HVDC cable. The corresponding operating points are those where a rectifier curve crosses the inverter curve, i.e. they are coupled at V_{Rdc}.

The inverter curve (E_I = constant) considers that the VSC inverter controls the HVDC voltage E_I. The WPP can control the off-shore ac-grid voltage (V_{Fd} = constant curves) or allow WT optimal tracking (P_F = constant curves). The analyzed scenarios with increasing complexity are:
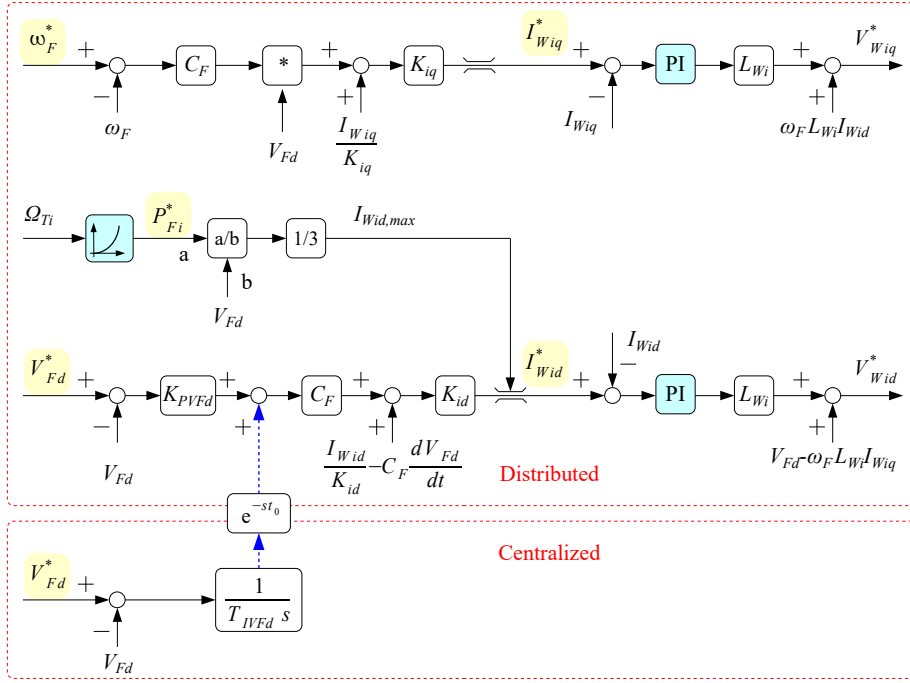
Figure 3: Front-end control loops of the aggregated wind turbine i, $i = 1, 2, .., 5$.

1. Islanded WPP with voltage control (with or without centralized secondary control, which requires communications).
2. Diode rectifier conducting and WPP providing voltage control.
3. Diode rectifier conducting and WPP providing active power control with both: a) Point-to-point system, and b) Multi-terminal system.

3. Point-to-point System

In this section the off-shore WPP is connected to the on-shore ac-grid through an HVDC link, with a diode based rectifier station. The corresponding analysis of scenarios 1, 2 and 3.a is outlined below.

3.1. Scenario 1: Islanded Wind Power Plant

In scenario 1, the WT grid converters control the voltage and the frequency of the off-shore ac-grid, according with the diagrams shown in Figure 3. These control strategies have been validated in [4] and [8]. The WPP model is expressed in a synchronous rotating frame aligned with the collector voltage V_F, i.e., $V_{Fq} = 0$.

The WPP model considers the cable capacitance from the individual WTGs to PCC$_F$ to be lumped together with the capacitor bank C_F, whereas the inductive terms are neglected, as they would appear
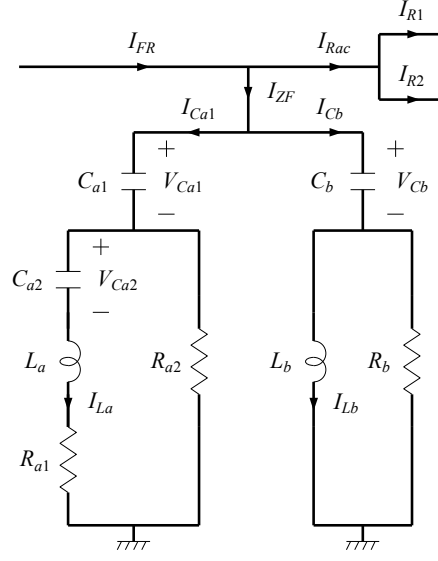
Figure 4: Rectifier ac-side Z_{FR} filter, according to [18].

in series with the much larger WT transformer leakage inductance. For a string of 10x5 MW WTs 1.5 km apart, this simplification corresponds to a maximum voltage error of 0.656 %. Regarding its dynamic effects, the simplification introduces a maximum angle difference corresponding to a delay of 77.6 μs. In any case, the sensitivity on the system dynamics to different delays and values of C_F is included in the following sections of the paper.

3.1.1. Model for Islanded Operation

The models for the islanded WPP small-signal analysis have been taken from [16] where 21 state space variables are defined for WPP (Figure 1) and rectifier ac-side filter (Figure 4):

$$[x]_{WPP} = [I_{Wid}, I_{Wiq}, V_{Fd}, \ V_{Ca1,dq}, V_{Cb,dq}, V_{Ca2,dq}, I_{La,dq}, I_{Lb,dq}]^t$$

The integral term of the voltage control error (Figure 3) requires a centralized calculation, and a $t_0 = 10$ ms communication delay is applied to each of the WTs. This communication delay is common for modern large distance industrial busses used for WPP control and is similar to that in distributed systems such as protective relay systems, where the communication delay is usually less than 10 ms, [19, 20]. A granularity of 1 ms is desired for communication delay sensitivity studies, therefore, the system is analyzed in the discrete domain using a sampling period $T_m = 1$ ms, and $r = t_0/T_m = 10$ new state-space variables are added:

$$[x]_{VF} = [x_{Fd}, x_1, x_2, .., x_r]^t$$

7

where x_{Fd} is the state-space variable associated with the centralized integrator and $x_1, x_2, .., x_r$ are used for the discrete domain modeling. The state variables corresponding to the integral states of the current PI controllers (Figure 3) are $[x]_{IW} = [x_{Wid}, x_{Wiq}]^t$.

The state equations corresponding to the above 42 state variables are shown and validated in [16], and will not be repeated here, for the sake of brevity. Therefore, only the dynamic equations required for the new studies will be included, as the HVDC rectifier filter Z_{FR}, Figure 4:

$$I_{FRq} = I_{Laq} - \frac{1}{R_{a2}} V_{Ca1q} + I_{Lbq} - \frac{1}{R_b} V_{Cbq} + I_{Racq} \tag{1}$$

and the voltage control loop, Figure 3:

$$I_{Wid}^* = \{K_{PVFd} C_F (V_{Fd}^* - V_{Fd}) + \frac{C_F}{T_{IVFd}} x_{VFd} + I_{FRd}\} K_{id} \tag{2}$$

$$\frac{dx_{VFd}}{dt} = V_{Fd}^* - V_{Fd} \tag{3}$$

3.1.2. Small-signal Stability Analysis with Centralized Voltage Control

In [16] the WPP model is validated, considering a non-constant off-shore ac-grid frequency for accurate dynamic behavior:

$$\omega_F = \frac{1}{C_F V_{Fd}} \sum_i I_{Wiq} - \frac{1}{C_F V_{Fd}} I_{FRq} \tag{4}$$

Figure 5 shows the discrete root locus plot for different communication delays (1, 3, 5, 7, 10, 12, 15, 17, 20, 22 and 25 ms). With the controller designed for a nominal 10 ms delay, the system becomes unstable if actual communication delay is 20 ms or more. The PSCAD simulation shown in Figure 6 for different communication delays shows instability for 20 ms delay, thus validating the root locus analysis.

3.1.3. Islanded Operation not requiring Communication

A centralized controller designed for accurate voltage tracking in islanded operation might lead to instability for large communication delays. Alternatively, communication delay can be avoided by just using the local proportional voltage regulators in Figure 3. In this case, no communication is required, at the expense of ac-grid steady-state voltage errors.

Equation (2) becomes:

$$I_{Wid}^* = \{K_{PVFd}' C_F (V_{Fd}^* - V_{Fd}) + I_{FRd}\} K_{id} \tag{5}$$

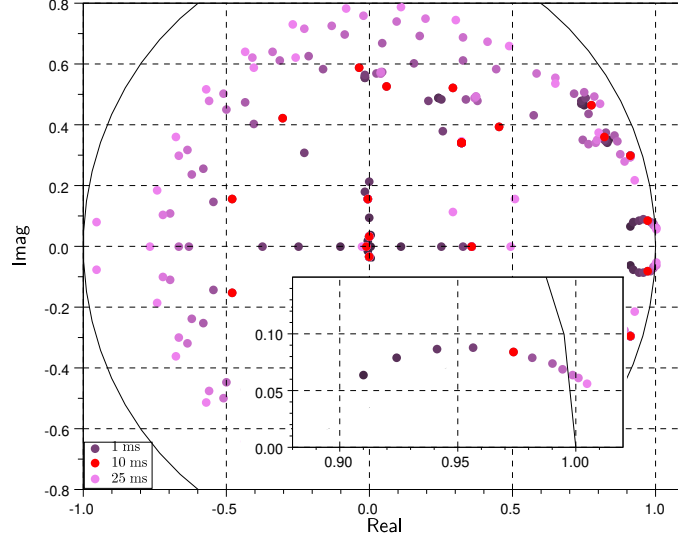and equation (3) together with state-space variables $[x]_{VF}$ no longer apply.

Figure 5: Root locus of the islanded WPP as a function of the centralized voltage control delay (z-plane).
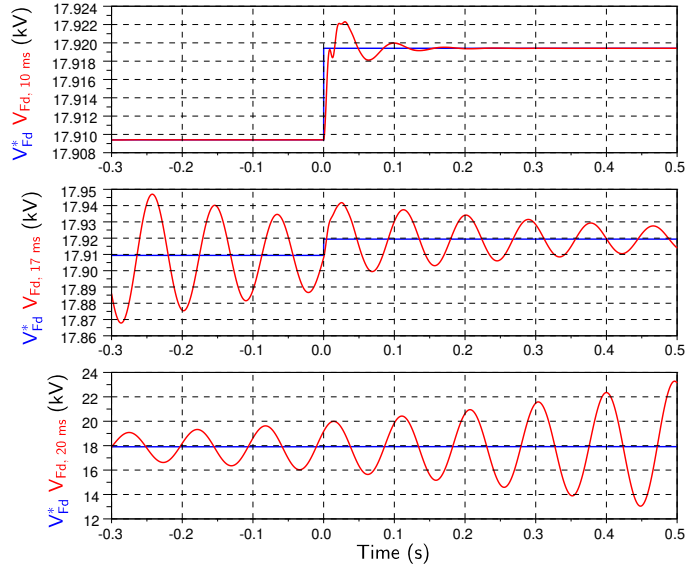

Figure 6: Islanded WPP response to a V_{Fd}^* step as a function of the communication delay (10, 17 and 20 ms).

The new model is validated comparing the analytical small-signal response with that of PSCAD simulations. The frequency reference is $\omega_F^* = 2\pi 50$.

The new controller performance is shown in Figure 7, where the responses of the system linearized assuming ω_F being a constant equal to 50 Hz and linearized considering ω_F as a variable are compared with the PSCAD EMT results. The traces show the voltage V_{Fd} and WT current I_{W5} responses to a 10 V step in V_{Fd}^*. Figure 7 shows an excellent agreement between the variable frequency analytical
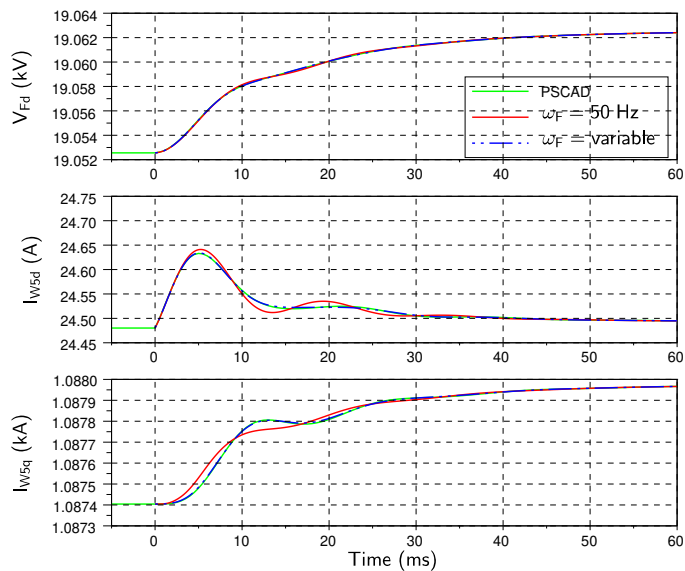
9

Figure 7: Islanded WPP response to a V_{Fd}^* step for model validation.

response and the PSCAD simulation.

The stability analysis and robustness of the islanded WPP with the voltage control without communication is carried out by the corresponding root locus analysis. Figure 8 shows the root locus plot for a set of C_F values, from 50 μF (dark) to 200 μF (light); the rated value is 93.5 μF. Since the diode rectifier is disconnected, sensitivity to Z_{FR} is not included in the analysis. Figure 8 uses a logarithmic scale to show clearly the closest roots to the right-half plane. A reduction on the value of the diode rectifier filter size (C_F) leads to eigenvalues closer to the right-half plane. Nevertheless, the system remains stable for the considered wide filter size range variation. The stability analysis has been carried out considering variable frequency ω_F and it is assumed that the value of C_F is estimated, so relevant controllers are re-tuned for each value of C_F.

3.2. Scenario 2. Diode Rectifier conducting and Wind Power Plant Voltage Control

Scenario 2 considers that the diode rectifier station is conducting. Therefore, the small-signal stability analysis includes the HVDC rectifier, the submarine HVDC cables, and the grid-forming WPP model developed in the previous section. The on-shore VSC inverter controls the HVDC voltage E_I, i.e., the HVDC link operates at point 2 of Figure 2.

3.2.1. Model for Connected Operation

The 100 km length submarine cables are modeled as in [16] using the equivalent T-model, and add three new state-space variables, $[x]_{cable} = [I_{Rdc}, E_C, I_{Idc}]^t$.
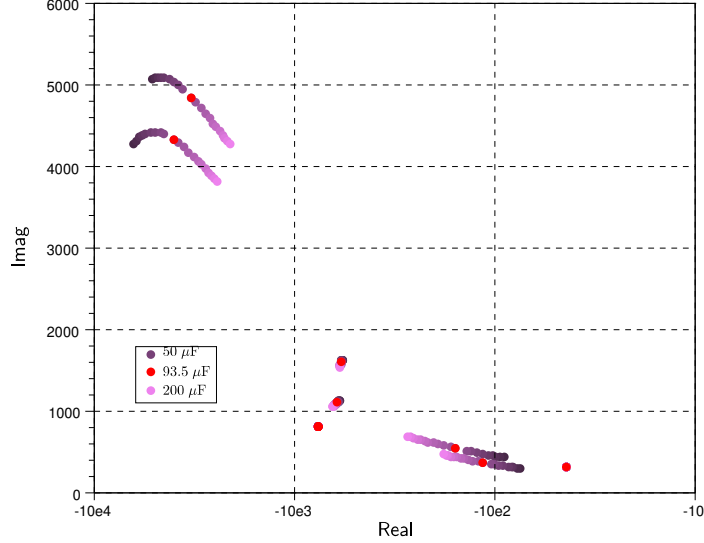
10

Figure 8: Root locus of the islanded WPP as a function of C_F.

The corresponding state space equations are shown in [16] together with the HVDC rectifier equations. The parameter values in this paper are: the number of 6-pulse poles is $B = 2$, the transformer ratio is $N = 122/33$ and the leakage transformer inductance L_{TR} is referred to the secondary side (122 kV). Note the rectifier equations in [16] are algebraic and depend on the non-stationary frequency ω_F.

3.2.2. Model Validation with Dynamic Rectifier Model

The analytical model is validated against a PSCAD EMT model which includes the 12 diode rectifier valves for a 12-pulse rectifier, together with their transformers, grading resistances and snubber circuits, based on the LCC station in the HVDC CIGRE benchmark model [18]. This detailed switching model is considered adequate for model validation and EMT dynamic simulations, [17, 21].

The model validation is carried out in [16] using an explicit expression for the non-constant offshore ac-grid frequency. However, the agreement of step response results in [16] with the corresponding PSCAD simulation is limited. Therefore, a dynamic, more accurate model of the diode rectifier is used in this paper, [22]:

$$V_{Rdc} = \frac{3\sqrt{6}}{\pi} B N V_{Fd} - \frac{3}{\pi} B \omega_F L_{TR} I_{Rdc} - 2 B L_{TR} \frac{dI_{Rdc}}{dt} \tag{6}$$

$$I_{Racd} = \frac{B\sqrt{6}}{\pi} N I_{Rdc} - \frac{B}{\pi} \frac{\omega_F L_{TR} I_{Rdc}^2}{V_{Fd}} \tag{7}$$

$$I_{Racq} = -\frac{N}{\sqrt{2}} \frac{B\sqrt{3}}{\pi} I_{Rdc} \sin\mu + 3 B N^2 \frac{V_{Fd}}{2\pi\omega_F L_{TR}} (\sin\mu - \mu) \tag{8}$$
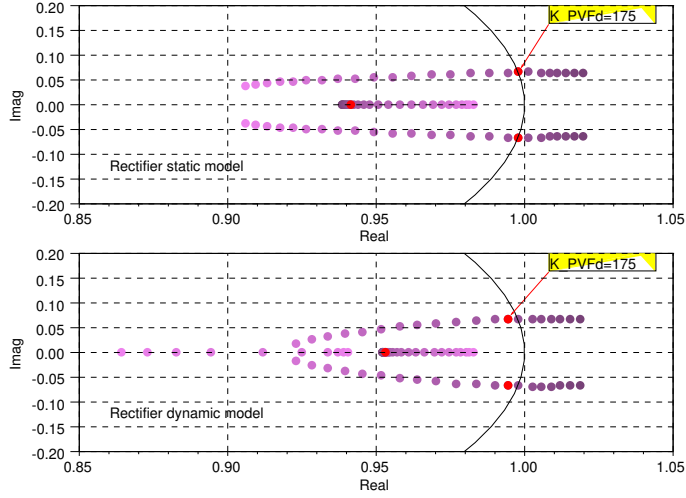
11

Figure 9: Root locus of the connected WPP as a function of K_{PVFd} from 20 (dark) to 1000 (light), (zoom).

where μ is the commutation angle of the diode rectifier:

$$\mu = \arccos\left(1 - \frac{2\omega_F L_{TR} I_{Rdc}}{\sqrt{6} N V_{Fd}}\right) \tag{9}$$

The dynamic term $2BL_{TR}\dot{I}_{Rdc}$ does not add any new state variable as it represents an inductor in series with L_R (see Figure 1).

The effect of the more accurate model in the small-signal analysis is shown in Figure 9, which shows the system root locus a function of the PI voltage controller proportional gain K_{PVFd} of the PI. K_{PVFd} values go from 20 (dark) to 1000 (light). Only the roots more critical to stability are shown. With the rectifier static equations used in [16] the system is unstable for $K_{PVFd} = 175$, however, using the dynamic diode rectifier model, the system is shown to be stable down to $K_{PVFd} = 150$, which is the correct answer. There is also a small improvement in computing the operating point for the system linearization, Appendix B

To validate the considered system, a PSCAD simulation is compared with the analytic results obtained using both the static and the dynamic diode rectifier models for a 10 V step in the ac-grid voltage reference (V_{Fd}^*). Results are shown in Figure 10 for $K_{PVFd} = 175$. Traces have been filtered with a first order low pass filter with a 2 ms time constant to reduce the ripple caused by the diode rectifier in the PSCAD solution (only for representation purposes). Clearly, the diode dynamic equations improve the agreement between analytical and PSCAD simulation results.

The variable frequency ω_F can be obtained by substituting (1) and (8) into (4), however, an explicit expression for ω_F cannot be obtained from the resulting equation because of the use of more complex
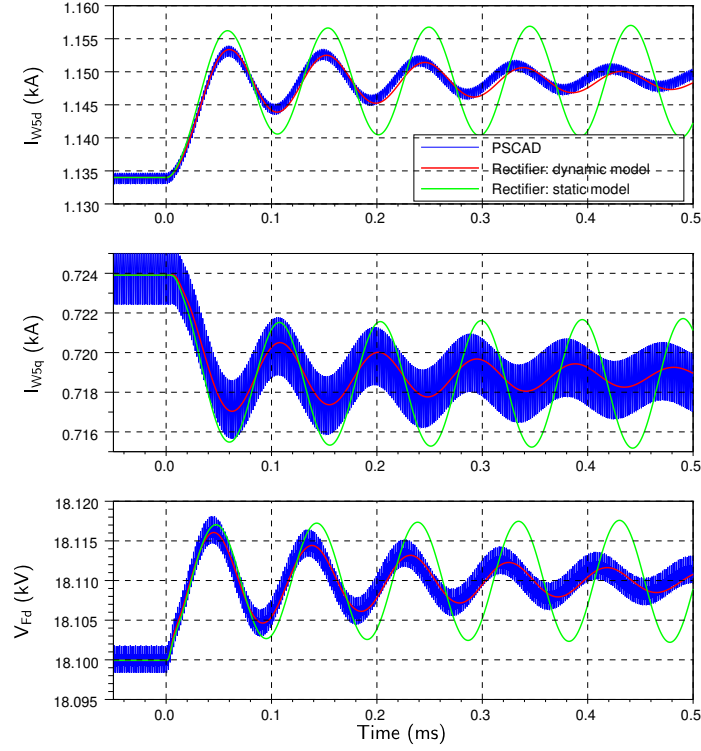
Figure 10: WPP and DR response to a V_{Fd}^* step for model validation (filtered).

rectifier model. Therefore, an implicit expression for ω_F has been obtained after linearization:

$$
\begin{aligned}
\Delta\omega_F = \frac{-1}{K_{80}} \Bigg\{ &\frac{1}{K_{5q}} \Delta I_{W5q} + \left(\frac{3BN^2}{2\pi\omega_{F0}L_T} \arccos\left(K_{82}\right) - \omega_{F0}C_F - \frac{3BN^2 K_{81}}{2\pi\omega_{F0}L_T} - \right.\\
&\frac{\sqrt{6}BN}{2\pi V_{Fd0}} \frac{I_{Rdc0}}{\sqrt{1-K_{82}^2}} + \frac{\sqrt{6}BN}{4\pi} \cdot \frac{I_{Rdc0}\omega_{F0}K_{83}}{V_{Fd0}K_{81}} - \frac{3BN^2}{4\pi L_T} \frac{K_{83}}{K_{81}} \Bigg) \Delta V_{Fd} + \\
&\frac{1}{R_{a2}} \Delta V_{Ca1q} - \Delta I_{Laq} + \frac{1}{R_b} \Delta V_{Cbq} - \Delta I_{Lbq} + \left(\frac{\sqrt{6}BN}{2\pi\sqrt{1-K_{82}^2}} + \frac{\sqrt{6}BNK_{81}}{2\pi} - \right.\\
&\left. \frac{\sqrt{6}BN}{4\pi} \frac{\omega_{F0}K_{83}}{K_{81}} + \frac{3BN^2}{4\pi L_T} \frac{V_{Fd0}K_{83}}{I_{Rdc0}K_{81}} \right) \Delta I_{Rdc} \Bigg\}
\end{aligned}
\tag{10}
$$

where:

$$
\begin{aligned}
K_{80} = &\frac{\sqrt{6}BNI_{Rdc0}}{2\pi\omega_{F0}\sqrt{1-K_{82}^2}} - V_{Fd0}C_F - \frac{3BN^2}{2\pi L_T} \frac{V_{Fd0}}{\omega_{F0}^2} \cdot \\
&\left(K_{81} + \arccos K_{82} \right) - \frac{\sqrt{6}BN}{4\pi} \frac{I_{Rdc0}K_{83}}{K_{81}} + \frac{3BN^2}{4\pi L_T} \frac{V_{Fd0}K_{83}}{\omega_{F0}K_{81}}
\end{aligned}
\tag{11}
$$

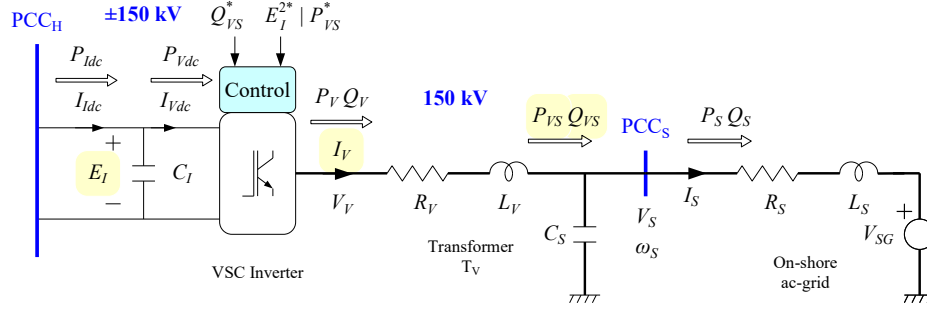13

Figure 11: HVDC VSC inverter connected to the on-shore ac-grid.

$$K_{81} = \sqrt{\frac{2\sqrt{6}L_T}{3N}\frac{\omega_{F0}I_{Rdc0}}{V_{Fd0}} - \frac{2}{3}\left(\frac{L_T}{N}\frac{\omega_{F0}I_{Rdc0}}{V_{Fd0}}\right)^2} \tag{12}$$

$$K_{82} = 1 - \frac{\sqrt{6}L_T}{3N}\frac{\omega_{F0}I_{Rdc0}}{V_{Fd0}} \tag{13}$$

$$K_{83} = \frac{4L_T^2}{3N^2}\frac{\omega_{F0}I_{Rdc0}^2}{V_{Fd0}^2} - \frac{2\sqrt{6}L_T}{3N}\frac{I_{Rdc0}}{V_{Fd0}} \tag{14}$$

3.3. Scenario 3a. Point-to-point System

In scenario 3a, the models of the on-shore VSC station and the on-shore ac-grid are included. In this case, the WT reference currents I_{Wid}^* are saturated and the front-end converters are in optimum P_{Fi} power tracking, Figure 3. Therefore the variables $[x]_{VF}$ are no longer state variables as the off-shore ac-grid voltage PI controller V_{Fd} is now saturated.

3.3.1. HVDC VSC Inverter Model and Control

Figure 11 shows the HVDC VSC inverter and the on-shore network which is modeled as its Thevenin equivalent (R_S, L_S and V_{SG}). The new state-space variables are:

$$[x]_{VSC} = \left[E_I^2, I_{Vd}, I_{Vq}, V_{Sd}, I_{Sd}, I_{Sq}\right]^t$$

Note that now E_I is a state variable. State equations can be found in Appendix A.

In the point-to-point system, the WT grid converters control the off-shore ac-grid frequency ω_F and the active power P_{Fi}, $i = 1, 2, .., 5$, of each WT. Hence, their control references are $[u]_{\omega F} = [\omega_F^*]$ and $[u]_{PF} = [P_{Fi}^*]$.

Figure 12 shows the HVDC voltage E_I and reactive power Q_{VS} control loops. The control inputs are $[u]_{VSC} = \left[E_I^{2*}, Q_{VS}^*\right]^t$ and the corresponding equations are shown in Appendix A.
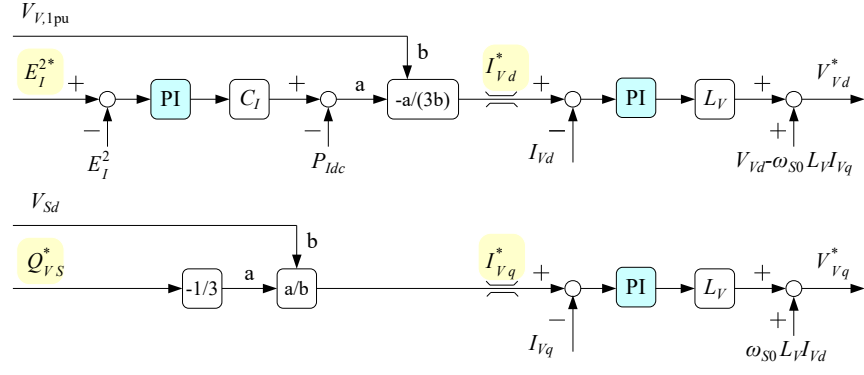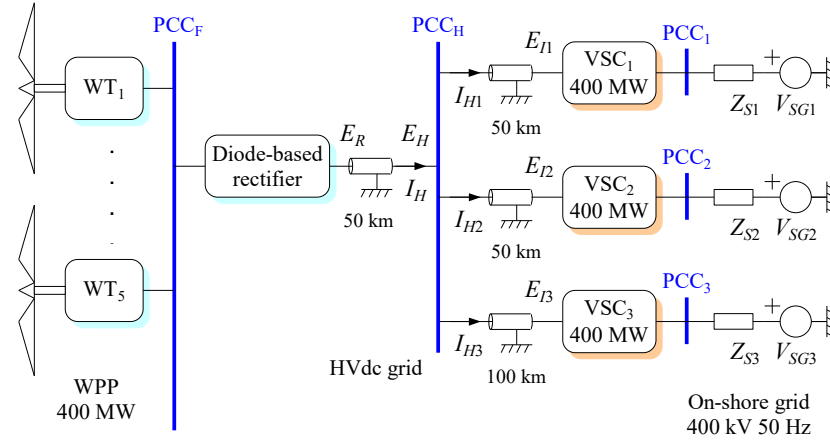
14

Figure 12: HVDC VSC control loops.

Figure 13: Diode-based rectifier for the connection of the WPP to the multi-terminal HVDC grid.

4. Scenario 3b. Multi-terminal System

In scenario 3b, a four terminal HVDC grid connects the WPP with three on-shore VSCs, Figure 13, as the one shown in Figure 11 and analyzed in Appendix A. During normal operation the WPP controls the ac-grid frequency and the active powers P_{Fi}, $i = 1, 2, .., 5$, whereas the VSCs control the reactive powers Q_{VSj}, $j = 1, 2, 3$. VSC-2 controls the active power P_{VS2} and the HVDC voltage is controlled by VSC-1 and VSC-3 using voltage control droop.

The coordinated design of the WT and HVDC link has shown that the diode-based HVDC rectifier can be used in a droop-controlled HVDC grid which minimizes the HVDC grid losses, [9].

4.1. Model of the Multi-terminal System

This section analyzes what is new regarding the former point-to-point system. The submarine cables are modeled as in [16] using the equivalent T-model and the associated state-space variable

$[x]_{cable}$ changes to:

$$[x']_{cable} = [I_{Rdc}, E_C, I_H, I_{Idc,j}, E_{C,j}, I_{H2}, I_{H3}]^t$$

I_{H1} is not considered as state-variable as it is a function of I_H, I_{H2} and I_{H3}.

Regarding the multi-terminal control, the WPP input controls are $[u]_{\omega F}$ and $[u]_{PF}$ whereas VSC-j input controls change to $[u']_{VSC} = \left[P^*_{VS2}, Q^*_{VSj}\right]^t$.

Therefore the former current reference I_{Vd} in Figure 12 and equation (A.11) changes to:

$$I^*_{V2d} = \frac{1}{3V_{S2d}} P^*_{VS2} \tag{15}$$

VSC-1 and VSC-3 use voltage droop control to keep the HVDC grid voltage close to 1 pu:

$$I^*_{Vdc1,3} = k_{droop1,3} \left(E_{I1,3} - E_{Ilow1,3}\right) \tag{16}$$

and PI controllers are used to control the currents $I^*_{Vdc1,3}$:

$$I^*_{Vd1,3} = K_{Pdroop1,3} \left(I^*_{Vdc1,3} - I_{Vdc1,3}\right) + \frac{1}{T_{Idroop1,3}} x_{droop1,3} \tag{17}$$

where:

$$\frac{dx_{droop1,3}}{dt} = I^*_{Vdc1,3} - I_{Vdc1,3} \tag{18}$$

The state-space variable $[x]_{PI,VSC}$ associated with the PI controller integrators changes to:

$$[x']_{PI,VSC} = [x_{Vd}, x_{Vq}, x_{droop1,3}]^t$$
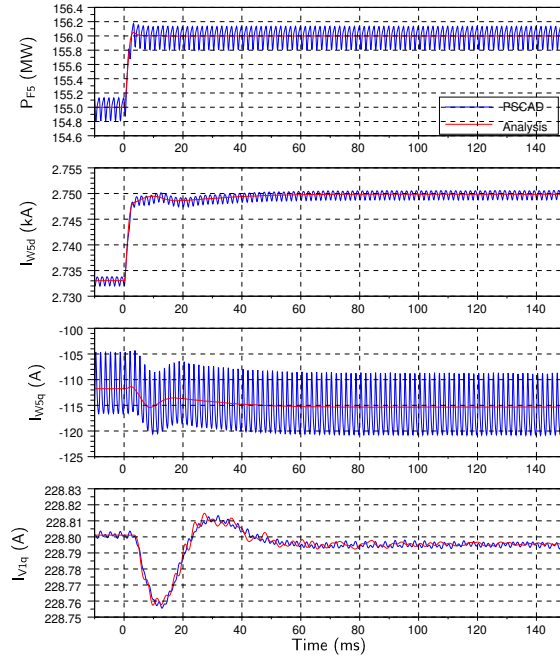
4.2. Model Validation

The small-signal analysis of the multi-terminal system is validated comparing the step responses with that of PSCAD simulation. Figure 14(a) shows the system responses (active power and currents at WT-5, and reactive current at VSC-1) to a 1 MW step in the active power P^*_{F5}. The initial operating point is: $P^*_{Fi} = 1$ pu, $\omega^*_F = 50$ Hz, $Q^*_{VSj} = -0,15$ pu and $P^*_{VS2} = 0,25$ pu, where $i = 1, 2, .., 5$ and $j = 1, 2, 3$.

Figure 14(a) compares the analytical model with PSCAD simulation when the HVDC T-cable model is used in PSCAD. The analytical results agree with that of PSCAD. Note the exact match in the VSC current I_{V1q}.

The same system response results are shown in Figure 14(b) but using the distributed parameter and frequency dependent cable model in PSCAD. Cable geometry and material properties are shown in [9].

16
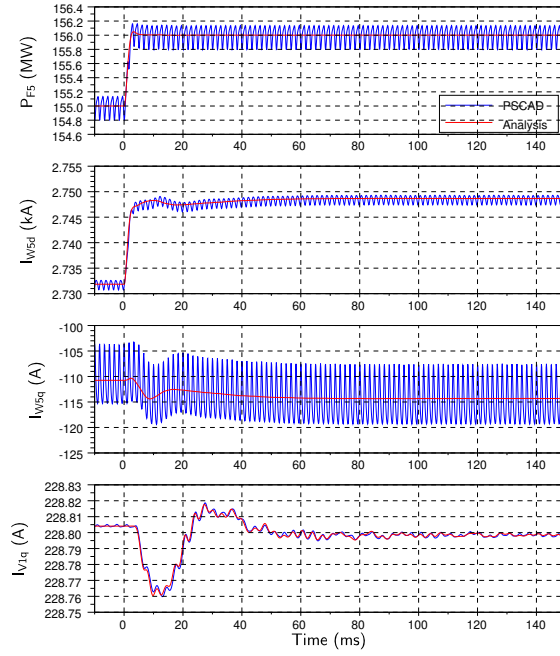
(a) HVDC cable with lumped parameters

(b) HVDC cable with distributed parameters

Figure 14: Multi-terminal system response to a P_{F5}^* step for model validation (filtered, 1 ms low pass filter).

Again the analytical results agree with that of PSCAD, hence validating the proposed multi-terminal system model, including the T-cable model.
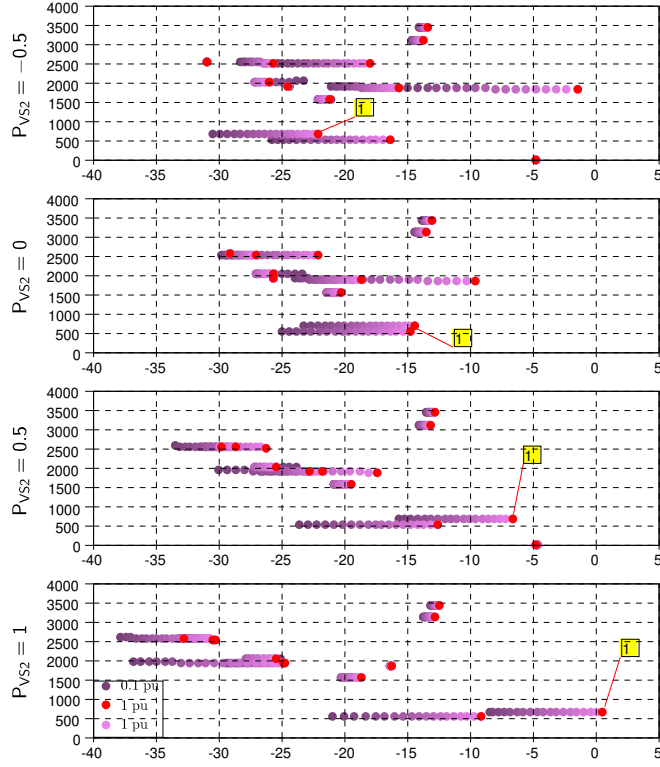
Figure 15: Root locus of the Multi-terminal system as a function of P_{Fi} and P_{VS2} (zoom).

4.3. Small-signal Stability Analysis

This section analyzes the small-signal stability of the multi-terminal system for the full range of operating points. Figure 15 shows the root locus of the multi-terminal system for a set of P_{Fi} values, from 0.1 pu (dark) to 1 pu (light), with a step value of 0.05 pu. The set of active power values of VSC-2 is $P_{VS2} = -0.5, 0, 0.5$ and 1 pu. It only shows the closest roots to the right-half plane. If P_{VS2} increases, the root marked with "1" moves toward the right-half plane and the stability analysis shows that the system is stable for all operating points except when $P_{VS2} = 1$ pu and P_{Fi} is close to 1 pu.

To make the multi-terminal system stable for the full range of operating points, the slope of the droop control can be increased, albeit the HVDC voltage shift will increase. Figure 16 shows the root locus of the multi-terminal system as a function of a constant K_3, from 0.5 (dark) to 2 (light), with a step value of 0.125. The droop constants are:

$$k_{droop1} = 2k_{droop3} = 0.11111K_3 \tag{19}$$

The red dots are the roots when the active powers are $P_{Fi} = 1$ pu and $P_{VS2} = 1$ pu, and the droop constants have their initial values, i.e., $K_3 = 1$. Figure 16 shows that with K_3 equal or greater
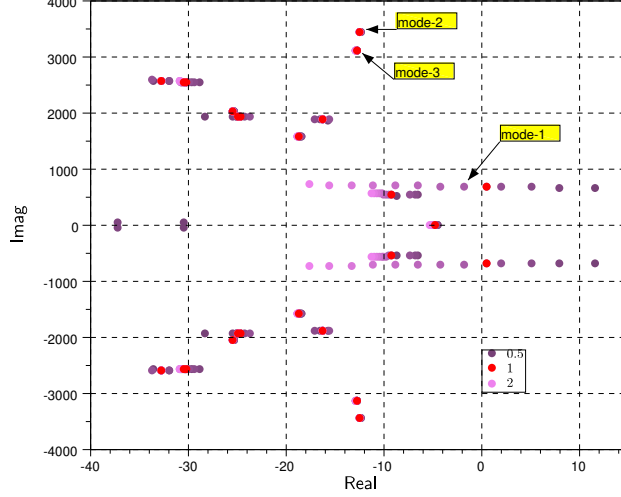
Figure 16: Root locus of the Multi-terminal system as a function of K_3 (zoom).

Table 1: Oscillatory modes and participation factors

Mode	Damping ratio (%)	Frequency (Hz)	Participation factors (%)
1	0.25	110.4	E_{I1}^2 (0.33), I_{H2} (0.24), x_{V2q} (0.19), I_{Idc1} (0.11), I_{Idc2} (0.10)
2	0.36	547.6	E_{C1} (0.24), E_{C2} (0.24), I_{H2} (0.23), I_{Idc1} (0.14), I_{Idc2} (0.13)
3	0.41	497.2	E_{C2} (0.20), E_{C1} (0.20), I_H (0.18), I_{Idc2} (0.14), I_{Idc1} (0.14), E_C (0.07)
4	0.87	299.4	I_{S2q} (0.55), E_{I2}^2 (0.45), I_{V2q} (0.39), V_{S2d} (0.14), I_{S2d} (0.12)
5	1.18	407.3	I_{S3q} (0.25), V_{S3d} (0.25), I_{S3d} (0.25), θ_3 (0.22)
6	1.18	250.9	E_{C3} (0.31), I_{Idc3} (0.27), E_C (0.09), I_{H3} (0.07)
7	1.19	407.5	I_{S1q} (0.25), V_{S1d} (0.25), I_{S1d} (0.25), θ_1 (0.22)
8	1.25	324.6	E_C (0.32), I_H (0.22), E_{C3} (0.12), I_{H3} (0.12)
9	1.27	411.3	V_{S2d} (0.36), I_{S2d} (0.32), I_{S2q} (0.20), E_{I2}^2 (0.13), I_{V2q} (0.11)
10	1.28	306.9	θ_3 (0.25), I_{S3d} (0.22), V_{S3d} (0.22), I_{S3q} (0.22)
11	1.29	307.0	θ_1 (0.25), I_{S1d} (0.22), V_{S1d} (0.22), I_{S1q} (0.22)
12	1.72	87.4	E_{I3}^2 (0.31), I_{H3} (0.24), I_{Idc3} (0.15), x_{V2q} (0.14)
13	13.80	50.0	V_{Ca2q} (0.47), V_{Ca2d} (0.47)
14	31.98	191.9	I_{Laq} (0.27), V_{Ca1d} (0.26), I_{Lad} (0.23), V_{Ca1q} (0.20), I_{W5q} (0.10)

than 1.125 the system becomes stable, so the value of $K_3 = 1.25$ is chosen for the voltage droop control, whereas (19) ensures the HVDC optimal operation, [9].

4.4. Participation Factors

Table 1 shows the oscillatory modes with the smallest damping ratios, when $P_{Fi} = 1$ pu, $P_{VS2} = 1$ pu and $K_3 = 1.125$. From Table 1, modes 1, 2 and 3 exhibit the lowest dampings (0.25%, 0.36% and 0.41% respectively), and are represented in Figure 16. The main contributors to these modes are the HVDC grid state variables ($E_{I1}^2, I_H, I_{H2}, E_{C1}, E_{C2}, I_{dc1}, I_{dc2}$).

Figure 17 shows the eigenvalues gathered according to Table 1. Clearly, impact of HVDC control on system stability is much more relevant than the impact of the diode rectifier unit (DRU) connected WPP. Therefore, HVDC voltage droop control has great impact on system damping and reinforces the solution proposed in section 4.1.
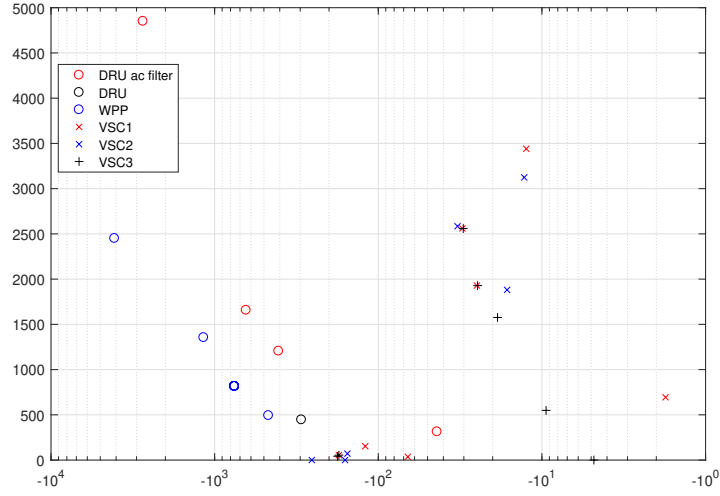
Figure 17: Eigenvalues classified according to participation factors.

5. Conclusions

This paper has shown the small signal stability analysis of a hybrid LCC-VSC HVDC system consisting on a diode rectifier based WPP connected to a multi-terminal HVDC grid. The developed models have been carefully validated against PSCAD EMT simulations including detailed switching models of the diode rectifier converter station.

It has been shown that the use of a variable off-shore grid frequency in the dynamic models improves the accuracy of the small-signal stability analysis. Moreover, an averaged dynamic model of the diode rectifier station also improves the results, albeit a more complex expression of the variable off-shore frequency has to be used.

The developed small signal stability analysis has shown that WT converter control has an important influence on overall system stability and should be taken into account for HVDC grid stability analysis when DR converters are connected to the system.

When centralised controllers are used, robustness to communication delays need to be studied. To avoid the problems caused by communication delay, a voltage control strategy that does not require communication has also been introduced and validated.

The considered HVDC multi-terminal system includes a DR-connected WPP, one VSC terminal operating with constant power reference and two VSC terminals operating in voltage droop control.

A sensitivity analysis has been carried out for different operating points. For increasing WPP delivered power the overall damping decreases, leading, in some cases, to instability.

The participation factor analysis of oscillatory modes with lowest damping has shown that the HVDC voltage droop control parameters have great impact on the system stability. Therefore, the droop constants are increased to avoid stability issues, though leading to greater HVDC grid voltage

excursion for different power levels.

The fact that HVDC droop control has a large direct impact on overall system stability with adequately tuned WT converter controls is not surprising, as dc-side dynamics are generally faster than ac-side dynamics. However, this result is not obvious, as the DR is a passive element with strong ac-dc side coupling. This result has the important practical implication that the initial WT converter control can be designed without a detailed knowledge of the HVDC grid dynamics, which, in all cases, must be followed by a full stability analysis of the complete wind power plant and HVDC grid .

Acknowledgments

Appendix A. VSC Model and Control

Phase-A of the equivalent voltage source V_{SG} in Figure 11 is $V_{SG,A}(t) = |V_{SG}| \cos \theta_{SG}(t)$ where $\theta_{SG}(t) = \omega_{S0} \cdot t$ and $\omega_{S0} = 2\pi 50$. From the dynamic equation of the capacitor C_I and the power balance of the VSC, neglecting losses, the state equation of E_I^2 is hence obtained:

$$E_I I_{Idc} - 3V_{Vd}I_{Vd} - 3V_{Vq}I_{Vq} = \frac{C_I}{2}\frac{dE_I^2}{dt} \tag{A.1}$$

The state equations of the T_V transformer currents (I_{Vd} and I_{Vq}) are:

$$V_{Vd} = R_V I_{Vd} + L_V \frac{dI_{Vd}}{dt} - \omega_S L_V I_{Vq} + V_{Sd} \tag{A.2}$$

$$V_{Vq} = R_V I_{Vq} + L_V \frac{dI_{Vq}}{dt} + \omega_S L_V I_{Vd} + V_{Sq} \tag{A.3}$$

expressed on a synchronous frame rotating at ω_S and oriented on V_S, i.e., $V_{Sq} = 0$. V_{Vd} and V_{Vq} are the control variables in (A.13) and (A.14).

The state equation of V_{Sd} can be found from equations of capacitor C_S:

$$I_{Vd} - I_{Sd} = C_S \frac{dV_{Sd}}{dt} \tag{A.4}$$

$$I_{Vq} - I_{Sq} = \omega_S C_S V_{Sd} \tag{A.5}$$

21

The state equations of I_{Sd} and I_{Sq} are obtained from the on-shore ac-grid Thevenin's equivalent:

$$V_{Sd} = R_S I_{Sd} + L_S \frac{dI_{Sd}}{dt} - \omega_S L_S I_{Sq} + V_{SGd} \tag{A.6}$$

$$0 = R_S I_{Sq} + L_S \frac{dI_{Sq}}{dt} + \omega_S L_S I_{Sd} + V_{SGq} \tag{A.7}$$

$$V_{SGd} = |V_{SG}| \cos(\theta_{SG} - \theta_S) \tag{A.8}$$

$$V_{SGq} = |V_{SG}| \sin(\theta_{SG} - \theta_S) \tag{A.9}$$

θ_S is a new state-space variable $[x]_{\theta S} = [\theta_S]$ and the corresponding state equation can be obtained from (A.5):

$$\frac{d\theta_S}{dt} = \omega_S = \frac{1}{C_S V_{Sd}} I_{Vq} - \frac{1}{C_S V_{Sd}} I_{Sq} \tag{A.10}$$

From the outer control loops in (Figure 12):

$$I_{Vd}^* = \left\{ K_{PEI} \left(E_I^{2*} - E_I^2 \right) + \frac{1}{T_{IEI}} x_{EI} - \frac{I_{Idc0}}{2E_{I0}} E_I^2 - E_{I0} I_{Idc} \right\} \frac{-1}{3V_{V,1pu}} \tag{A.11}$$

$$I_{Vq}^* = \frac{-1}{V_{Sd}} Q_{VS}^* \tag{A.12}$$

where $V_{V,1pu} = 150/\sqrt{3}$ kV.

Assuming an ideal VSC, $V_{Vd} \approx V_{Vd}^*$ and $V_{Vq} \approx V_{Vq}^*$, then from the inner control loops shown in Figure 12:

$$V_{Vd} = K_{PVd} L_V \left(I_{Vd}^* - I_{Vd} \right) + \frac{L_V}{T_{IVd}} x_{Vd} - L_V I_{Vq} \omega_{S0} + V_{Sd} \tag{A.13}$$

$$V_{Vq} = K_{PVq} L_V \left(I_{Vq}^* - I_{Vq} \right) + \frac{L_V}{T_{IVq}} x_{Vq} + L_V I_{Vd} \omega_{S0} \tag{A.14}$$

The state-space variables associated with the PI controller integrators are:

$$[x]_{PI,VSC} = [x_{Vd}, x_{Vq}, x_{EI}]^t$$

and the corresponding state equations are:

$$\frac{dx_{Vd}}{dt} = I_{Vd}^* - I_{Vd} \;,\; \frac{dx_{Vq}}{dt} = I_{Vq}^* - I_{Vq} \;,\; \frac{dx_{EI}}{dt} = E_I^{2*} - E_I^2 \tag{A.15}$$

Appendix B. Steady-State Operation of the HVDC Diode Rectifier

Even though the DR model from equations (6)-(8) is named as "dynamic" model, the calculation of the overlap angle is more precise than the static model of [16], e.g., the estimation of the reactive
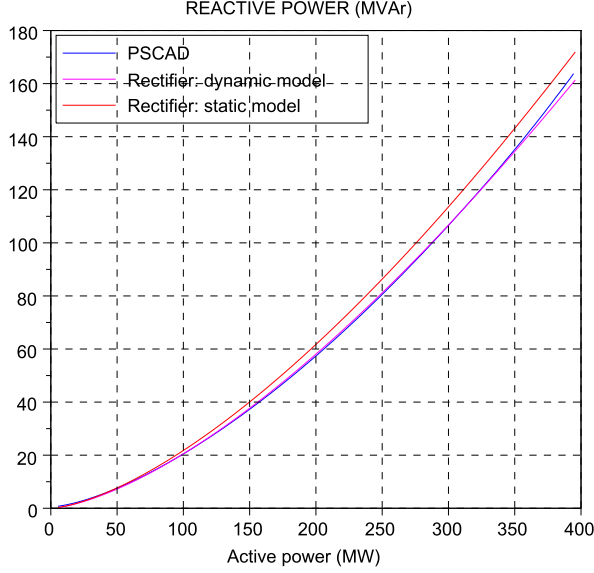
Figure B.18: Reactive power absorbed by the DR station.

Table C.2: System Parameters

Aggregated Wind Turbines
Front-end: 3.5 kVcc, 2 kVac, 50 Hz
T_{Wi}: 2/33 kV, $R_{Wi} = 0.005$ pu, $X_{Wi} = 0.06$ pu
Rated powers: 5, 40, 80, 120, 155 MVA
HVDC Rectifier (based on Cigre benchmark model [18])
Capacitor Bank: $C_F = 93.53$ μF
ZF-low frequency filter
$C_{a1} = 187.1$ μF, $C_{a2} = 2.079$ μF, $L_a = 4.879$ mH
$R_{a1} = 1.063$ Ω, $R_{a2} = 9.357$ Ω
ZF-high frequency filter
$C_b = 187.1$ μF, $R_b = 2.977$ Ω, $L_b = 0.4859$ mH
Transformer T_{R1} and T_{R2}
33/122 kV, 240+240 MVA, $X_{TR} = 0.18$ pu
dc-smoothing reactor: $L_R = 0.2$ H
HVDC Cable T-model (100 km)
$C_C = 11.57$ μF, $L_C = 60.89$ mH, $R_C = 1.691$ Ω
HVDC VSC and on-shore ac-grid
VSC: 300 kVcc, 400 MW, 150 kVac, 50 Hz, $C_I = 35.5$ μF
T_V: 150/400 kV, 440 MVA, $R_V = 0.024$ pu, $L_V = 0.17$ pu
ac-grid: 400 kV, 500 MVA, Scc = 6 pu, $\varphi_S = 80^o$

Table C.3: Control Parameters

Front-end Controller Parameters, Figure 3		
ac-voltage:	$K_{PVFd} = 203$	$T_{IVFd} = 68.966 \times 10^{-6}$
ac-voltage:	$K'_{PVFd} = 70$	
d-current:	$K_{PWid} = 1,488$	$T_{IWid} = 0.80645 \times 10^{-6}$
q-current:	$K_{PWiq} = 1,488$	$T_{IWiq} = 0.80645 \times 10^{-6}$
VSC PI Controller Parameters, Figure 12		
dc-voltage:	$K_{PEI} = 19.563$	$T_{IEI} = 7.6674 \times 10^{-3}$
d-current:	$K_{PVd} = 310.39$	$T_{IVd} = 29.318 \times 10^{-6}$
q-current:	$K_{PVq} = 310.39$	$T_{IVq} = 29.318 \times 10^{-6}$
VSC Droop Parameters		
VSC-1,3:	$k_{droop1} = 0.11111$	$k_{droop3} = 0.055556$

power absorbed by the DR converter is more precise. Figure B.18 shows the reactive power absorbed by the rectifier station as a function of the operating point and compares the analytical model results with that of the non-linear EMT model. The maximum 4.5 % error for the static model is reduced to 1.9 % with the dynamic model.

Appendix C. System Parameters

Table C.2 and Table C.3 show the parameter values of the system components and system controls.

References

[1] S. Chondrogiannis, M. P. Blanco, Market integration scheme of a multi-terminal hvdc grid in the north seas, IEEE Transactions on Power Systems 31 (3) (2016) 2415–2422. `doi:10.1109/TPWRS.2015.2465860`.

[2] S. S. Torbaghan, M. Gibescu, B. G. Rawn, M. v. d. Meijden, A market-based transmission planning for hvdc grid: Case study of the north sea, IEEE Transactions on Power Systems 30 (2) (2015) 784–794. `doi:10.1109/TPWRS.2014.2332762`.

[3] R. Blasco-Gimenez, S. Añó-Villalba, J. Rodríguez-D'Derlée, S. Bernal-Perez, F. Morant, Diode-based hvdc link for the connection of large offshore wind farms, Energy Conversion, IEEE Transactions on 26 (2) (2011) 615–626. `doi:10.1109/TEC.2011.2114886`.

[4] R. Blasco-Gimenez, S. Añó-Villalba, J. Rodríguez-D'derlée, F. Morant, S. Bernal-Perez, Distributed voltage and frequency control of offshore wind farms connected with a diode-based hvdc link, Power Electronics, IEEE Transactions on 25 (12) (2010) 3095–3105. `doi:10.1109/TPEL.2010.2086491`.

[5] R. Blasco-Gimenez, N. Aparicio, S. Añó-Villalba, S. Bernal-Perez, Lcc-hvdc connection of offshore wind farms with reduced filter banks, Industrial Electronics, IEEE Transactions on 60 (6) (2013) 2372–2380. `doi:10.1109/TIE.2012.2227906`.

[6] P. Menke, New grid access solutions for offshore wind farms, EWEA Off-shore (2015).
URL `http://www.ewea.org/offshore2015/conference/allposters/PO208.pdf`

[7] S. Seman, R. Zurowski, T. Christ, Investigation of dc converter nonlinear interaction with offshore wind power park s EWEA Off-shore (2015).
URL `http://www.ewea.org/offshore2015/conference/allposters/PO214.pdf`

[8] S. Bernal-Perez, S. Añó-Villalba, R. Blasco-Gimenez, J. Rodríguez-D'Derlée, Efficiency and fault ride-through performance of a diode-rectifier- and vsc-inverter-based hvdc link for offshore wind farms, Industrial Electronics, IEEE Transactions on 60 (6) (2013) 2401–2409. `doi:10.1109/TIE.2012.2222855`.

[9] S. Añó-Villalba, R. Blasco-Gimenez, S. Bernal-Perez, E. Belenguer, Wind power plant integration in voltage source converter hvdc grids with voltage droop control, Mathematics and Computers in Simulation 146 (2018) 186 – 199. `doi:https://doi.org/10.1016/j.matcom.2016.12.007`.

[10] L. Wang, K.-H. Wang, W.-J. Lee, Z. Chen, Power-flow control and stability enhancement of four parallel-operated offshore wind farms using a line-commutated hvdc link, Power Delivery, IEEE Transactions on 25 (2) (2010) 1190–1202. `doi:10.1109/TPWRD.2009.2034915`.

[11] L. Wang, K.-H. Wang, Dynamic stability analysis of a dfig-based offshore wind farm connected to a power grid through an hvdc link, Power Systems, IEEE Transactions on 26 (3) (2011) 1501–1510. `doi:10.1109/TPWRS.2010.2085053`.

[12] G. Pinares, M. Bongiorno, Modeling and analysis of vsc-based hvdc systems for dc network stability studies, IEEE Transactions on Power Delivery 31 (2) (2016) 848–856. `doi:10.1109/TPWRD.2015.2455236`.

[13] C. Guo, Z. Yin, C. Zhao, R. Iravani, Small-signal dynamics of hybrid lcc-vsc hvdc systems, International Journal of Electrical Power & Energy Systems 98 (2018) 362 – 372. `doi:https://doi.org/10.1016/j.ijepes.2017.12.010`.

[14] N. Chaudhuri, R. Majumder, B. Chaudhuri, J. Pan, Stability analysis of vsc mtdc grids connected to multimachine ac systems, Power Delivery, IEEE Transactions on 26 (4) (2011) 2774–2784. `doi:10.1109/TPWRD.2011.2165735`.

[15] G. Kalcon, G. Adam, O. Anaya-Lara, S. Lo, K. Uhlen, Small-signal stability analysis of multi-terminal vsc-based dc transmission systems, Power Systems, IEEE Transactions on 27 (4) (2012) 1818–1830. `doi:10.1109/TPWRS.2012.2190531`.

[16] S. Bernal-Perez, S. Ano-Villalba, R. Blasco-Gimenez, Stability analysis of HVDC-diode rectifier connected off-shore wind power plants, in: IECON 2015 - 41st Annual Conference of the IEEE Industrial Electronics Society, 2015, pp. 004040–004045. `doi:10.1109/IECON.2015.7392729`.

[17] M. . Cardiel-Álvarez, J. L. Rodriguez-Amenedo, S. Arnaltes, M. E. Montilla-DJesus, Modeling and control of lcc rectifiers for offshore wind farms connected by hvdc links, IEEE Transactions on Energy Conversion 32 (4) (2017) 1284–1296. `doi:10.1109/TEC.2017.2696261`.

[18] M. Szechtman, T. Wess, C. V. Thio, First benchmark model for hvdc control studies, Electra Vol. 135 (Num. 135) (1991) 54–73.

[19] Hongxia Wu, K. S. Tsakalis, G. T. Heydt, Evaluation of time delay effects to wide-area power system stabilizer design, IEEE Transactions on Power Systems 19 (4) (2004) 1935–1941. `doi:10.1109/TPWRS.2004.836272`.

[20] Schneider Electric, Easergy MiCOM P54x Current Differential Protection Relay: Technical Manual, P54x/EN M/Sh5 March, 2019.

[21] S. Chiniforoosh, H. Atighechi, A. Davoudi, J. Jatskevich, A. Yazdani, S. Filizadeh, M. Saeed-ifard, J. A. Martinez, V. Sood, K. Strunz, J. Mahseredjian, V. Dinavahi, Dynamic average modeling of front-end diode rectifier loads considering discontinuous conduction mode and unbalanced operation, IEEE Transactions on Power Delivery 27 (1) (2012) 421–429. `doi:10.1109/TPWRD.2011.2168983`.

[22] P. C. Krause, O. Wasynczuk, S. D. Sudhoff, S. Pekarek, Analysis of Electric Machinery and Drive Systems, 2nd Edition, IEEE Press Series in Power Engineering - John Wiley & Sons, Inc., 2002.